JCI The Journal of Clinical Investigation

Osimertinib activates a TGFβ2-dependent secretory program that drives lung adenocarcinoma progression

Madhurima Ghosh, Chao Wu, Abhishek Kumar, Monique B. Nilsson, John V. Heymach, Weina Zhao, Jiang Yu, Xin Liu, Na Ding, Shike Wang, Guan-Yu Xiao, Angelo Chen, Kate V. Grimley, William K. Russell, Chad J. Creighton, Xiaochao Tan, Jonathan M. Kurie

J Clin Invest. 2025. https://doi.org/10.1172/JCI198418.

Research In-Press Preview **Cell biology** **Clinical Research** **Oncology**

EGFR-mutant lung adenocarcinomas (LUADs) that are vulnerable to the EGFR antagonist Osimertinib (Osi) eventually relapse owing in part to the emergence of drug tolerant persister (DTP) cells that arise through epigenetic mechanisms. Intra-tumoral DTP cells can herald a worse clinical outcome, but the way in which DTP cells influence LUAD progression remains unclear. Osi-resistant (OR) cells exhibit typical DTP cell features, including a propensity to undergo senescence and epithelial-to-mesenchymal transition (EMT), which can activate heightened secretory states. Therefore, we postulated that OR cells influence LUAD progression through paracrine mechanisms. To test this hypothesis, we utilized congenic pairs of EGFR-mutant LUAD cell lines in which drug naive (DN) cells were rendered OR by chronic exposure to escalating doses of Osi. Co-cultured in vitro or co-injected into mice, paracrine signals from OR cells enhanced the growth and metastatic properties of DN cells. EMT and senescence activated non-overlapping secretomes, and OR cells governed DN cells by undergoing EMT but not senescence. Mechanistically, Osi rapidly increased TGFβ2 levels to initiate EMT, which triggered a Golgi remodeling process that accelerated the biogenesis and anterograde trafficking of secretory vesicles. The pro-tumorigenic activity of OR cells was diminished by depletion of EMT-dependent secreted proteins or the EMT-activating transcription factor ZEB1. These findings identify paracrine mechanisms by which OR cells drive LUAD progression.

Osimertinib activates a TGFβ2-dependent secretory program that drives lung adenocarcinoma progression

Madhurima Ghosh[1], Chao Wu[1], Abhishek Kumar[1], Monique Nilsson[1], John V. Heymach[1], Weina Zhao[1], Jiang Yu[1], Xin Liu[1], Na Ding[1], Shike Wang[2,3], Guan-Yu Xiao[4], Angelo Chen[5], Kate Grimley[6], William K. Russell[7], Chad J. Creighton[8], Xiaochao Tan[2,3*], Jonathan M. Kurie[1*]

[1]Department of Thoracic/Head and Neck Medical Oncology, The University of Texas–MD Anderson Cancer Center, Houston, Texas, USA. [2]Section of Hematology and Medical Oncology, Department of Medicine, Tulane University School of Medicine, New Orleans, Louisiana, USA. [3]Tulane Cancer Center, Louisiana Cancer Research Center, New Orleans, Louisiana, USA .[4]Department of Toxicology and Cancer Biology, The University of Kentucky, Lexington, Kentucky, USA. [5]Department of Biosciences, Rice University, Houston, Texas, USA. [6]Department of Chemistry, Texas A&M University, College Station, Texas, USA. [7]Department of Biochemistry and Molecular Biology, The University of Texas Medical Branch, Galveston, Texas, USA. [8]Department of Medicine and Dan L Duncan Comprehensive Cancer Center, Baylor College of Medicine, Texas, USA. *Co-correspondence: xtan4@tulane.edu; jkurie@mdanderson.org

Abstract

EGFR-mutant lung adenocarcinomas (LUADs) that are vulnerable to the EGFR antagonist Osimertinib (Osi) eventually relapse owing in part to the emergence of drug tolerant persister (DTP) cells that arise through epigenetic mechanisms. Intra-tumoral DTP cells can herald a worse clinical outcome, but the way in which DTP cells influence LUAD progression remains unclear. Osi-resistant (OR) cells exhibit typical DTP cell features, including a propensity to undergo senescence and epithelial-to-mesenchymal transition (EMT), which can activate heightened secretory states. Therefore, we postulated that OR cells influence LUAD progression through paracrine mechanisms. To test this hypothesis, we utilized congenic pairs of EGFR-mutant LUAD cell lines in which drug naive (DN) cells were rendered OR by chronic exposure to escalating doses of Osi. Co-cultured in vitro or co-injected into mice, paracrine signals from OR cells enhanced the growth and metastatic properties of DN cells. EMT and senescence activated non-overlapping secretomes, and OR cells governed DN cells by undergoing EMT but not senescence. Mechanistically, Osi rapidly increased TGFβ2 levels to initiate EMT, which triggered a Golgi remodeling process that accelerated the biogenesis and anterograde trafficking of secretory vesicles. The pro-tumorigenic activity of OR cells was diminished by depletion of EMT-dependent secreted proteins or the EMT-activating transcription factor ZEB1. These findings identify paracrine mechanisms by which OR cells drive LUAD progression.

Introduction

The term “oncogene addiction” was first coined to describe the reliance of cancer cells on a single mutated oncoprotein or pathway to maintain tumorigenicity (1). These driver mutations confer a growth advantage to cancer cells and form a rationale for the development of molecular targeted therapy (2). In 10-20% of patients with non-small cell lung cancer, activating mutations in *EGFR* serve as the driver mutation (3, 4). The two most frequently occurring “classical” EGFR mutations, exon 19 deletion mutations and L858R substitution mutations, constitute 85% of observed cases (3, 5). EGFR-selective tyrosine kinase inhibitors (TKIs) that reversibly bind to the ATP-docking site lead to rapid reductions in tumor bulk for LUAD patients harboring classical EGFR mutations (6). These findings support ongoing efforts to develop targeted therapies based on the oncogene addiction hypothesis.

Despite clear evidence of a survival benefit from reversible EGFR-TKI’s, tumors eventually regrow in patients who are on drug (7, 8). Acquired resistance can result from secondary EGFR mutations, including the gatekeeper T790M mutation (7, 8). To address acquired resistance to EGFR-TKI’s, Osimertinib (Osi) was developed (9, 10). Osi irreversibly binds to the ATP-binding domain of mutant EGFR proteins (6). Treatment regimens involving Osi have yielded highly effective short-term clinical outcomes, but acquired resistance to Osi eventually occurs and remains a major therapeutic challenge (8, 11). In most cases, acquired resistance to Osi is linked to the emergence of a population of drug tolerant persister (DTP) cells that arise through epigenetic mechanisms, are slow-cycling, possess a stem-like phenotype, and are prone to undergoing senescence and epithelial-to-mesenchymal transition (EMT) (12-17). DTP cells can either revert to an Osi-sensitive state or progress to a drug-tolerant expanded persister (DTEP) cell that exhibits heightened proliferative activity and can advance to an irreversible Osi-resistant (OR) state (18). DTP cells typically constitute a small fraction of total tumor bulk, but their presence predicts a poor clinical outcome (19, 20). Potentially underlying this observation,

senescent tumor cells acquire heightened secretory activity that can drive pro-metastatic processes in the tumor microenvironment (21-25). However, paracrine signals emanating from DTP cell populations have not been fully elucidated.

Proteins secreted through the conventional pathway are synthesized in the endoplasmic reticulum and then transported to the Golgi where they are sorted and packaged into secretory vesicles that are conveyed along microtubules to the plasma membrane (26). The conventional secretory pathway is constitutively activated in cancer by epigenetic events that accelerate secretory vesicle biogenesis (27-29). For example, senescence activates NFκB to initiate the senescence-associated secretory phenotype (SASP) (30, 31) and EMT-activating transcription factors upregulate the levels of phosphatidylinositol-4-kinase IIα (PI4K2A) and Rab6A to drive the biogenesis and anterograde trafficking of secretory vesicles (24, 25). Here, we postulated that heightened secretory states in DTP cells result from epigenetic events that underlie DTP cell outgrowth and play key roles in LUAD progression.

Results:

Secretory processes drive biological differences between drug-naïve (DN) and OR LUAD cells. To develop a model for hypothesis testing, we utilized human LUAD cell lines in which EGFR is constitutively activated owing to a deletion mutation (HCC827, ΔE746-A750) or missense point mutations (H1975, L858R/T790M). In monolayer culture, these cells demonstrated low-nanomolar Osi half maximal inhibitory (IC50) values (Fig.1 A-B). We treated them with escalating doses of Osi and found that, after 8 weeks of exposure, the emergent cells exhibited sharply higher Osi IC50 values (Fig. 1 A-B). For the purposes of this study, the emergent cells are designated as “OR” cells. The OR cells exhibited no evidence of secondary EGFR mutations by genomic sequencing (Fig. S1 A-B) or EGFR reactivation by western blot (WB) of EGFR pTyr (Y1068) (Fig. S1C-D), excluding oncogene reactivation as a basis for acquired resistance. Compared to DN cells, which were cuboidal and grew in clusters, OR cells were more dispersed and exhibited mesenchymal cell morphologies (Fig. S1E - G). Upon Osi withdrawal, OR cells partially regained sensitivity to Osi and/or underwent mesenchymal-to-epithelial transition (Fig. S1H-J), a plasticity consistent with a DTP cell phenotype. Thus, the congenic cell line pairs provided a model to elucidate epigenetic mechanisms by which Osi exposure causes DN cells to progress to an OR state.

Compared to DN cells, OR cells demonstrated lower proliferative activity in monolayer culture (Fig. S2 A-B), higher fractions of senescent cells based on β-galactosidase staining (Fig.S2 C-E), increased migratory and invasive activities in Boyden chambers (Fig. S2 F-I), and reduced tumorigenicity and metastatic activity in mice (Fig.1 C-E). The paradoxical finding that OR cells were more invasive but less metastatic than DN cells is consistent with prior reports (32) and raised the possibility that heterotypic cell-cell interactions govern OR cells in vivo. To test our hypothesis that heightened secretion underlies biologic features of OR cells, we asked whether secretory blockade is sufficient to reverse those features. In OR cells, short hairpin RNA (shRNA)-mediated depletion of Rab6A, a key driver of secretory vesicle biogenesis and transport (33), reduced Osi IC50 values, decreased the migratory and proliferative activities of OR cells, and attenuated β-galactosidase^{+} cell fractions (Fig. 1 F-J). Furthermore, treatment with Brefeldin A, which induces Golgi dispersal and inhibits secretion (34), reduced the proliferative and migratory activities of OR cells (Fig. 1 K, L). Lastly, we carried out conditioned medium (CM) transfer experiments and found that DN cells acquired features of OR cells following treatment with CM samples from OR, but not DN, cells (Fig. S3 A-F). These features included higher Osi IC50 values, reduced proliferative activity, and higher migratory activity (Fig. S3 A-F). Notably, the fraction of senescent cells only minimally increased in HCC827 DN cells (Fig. S3 G), suggesting that paracrine effectors are not sufficient to confer all DTP cell properties. These findings support the conclusion that secretion underlies certain biologic features of OR cells.

OR cells exert paracrine effects on DN cells in tumor models. In tumor samples derived from patients and pre-clinical models, the presence of DTP cells negatively impacts clinical outcome, yet DTP cells constitute a small fraction of total tumor bulk (19, 35). Based on the secretory phenotype exhibited by OR cells, we reasoned that paracrine signals from OR cells may influence the metastatic fate of surrounding tumor cells. To address this possibility, we generated tumors containing DN cells alone or a mixture of DN cells and OR cells (10:1 ratio) and found that tumors generated by OR:DN cell mixtures were larger and more metastatic (Fig. 2 A-C). To assess the extent to which paracrine effectors underlie this observation, we compared tumors generated by DN cells mixed with Rab6A-deficient or -replete OR cells and found that mixed-cell tumors generated by Rab6A-deficient OR cells were smaller and less metastatic (Fig. 2 D-F). These findings suggest that paracrine signals underlie the capacity of OR cells to drive LUAD progression.

Based on our finding that a fraction of OR cells were β-galactosidase$^+$, we reasoned that SASP may underlie the biologic differences between OR cells and DN cells. However, quantification of 48 different cytokines known to be SASP-associated showed that only 4 of them (IL-6, TNF-α, IP-10 and G-CSF) were present at higher concentrations in CM samples from OR cells than DN cells (Fig. 3 A). Because IL-6 and TNF-α can drive EMT and drug resistance (36, 37), we utilized genetic and pharmacogic approaches to block SASP (38, 39). Treatment with the JAK inhibitor Ruxolitinib (39) to block SASP reduced the levels of those secreted proteins but had no detectable effect on the proliferative or migratory properties of OR cells (Fig. 3 B-E). Similarly, mixed-cell tumors generated by DN cells and OR cells that were either NFkB-deficient or -replete were similar in size and metastatic activity (Fig. 3 F-H). Although these findings do not completely exclude a role for cytokine secretion, they suggest that SASP was not a major contributor to the biological properties of OR cells under these conditions.

Secretory mediators in OR cells. To more broadly assess the OR cell-derived secretome, we carried out liquid chromatography-mass spectrometry (LC-MS) on CM samples isolated from H1975-matched DN and OR cells. We identified a total of 580 proteins, 152 (26%) of which were present at markedly higher concentrations ($p< 0.05$, > 2-fold change) in CM samples from OR cells (Fig. 4 A). Gene Ontology analysis of the OR cell secretome revealed enrichment in terms such as 'regulation of cellular response to growth factor stimulus', 'regulation of cytokine production', 'inflammatory response', 'cell adhesion', 'blood vessel morphogenesis', and 'extracellular matrix organization' (Fig. S4 A). Among the upregulated proteins, collagen VI A1(COL6A1), L1 cell adhesion molecule (L1CAM), and cell migration inducing hyaluronidase (CEMIP) were of particular interest based on their correlations with shorter survival durations in TCGA LUAD cohort (Fig. S4 B-D) and reports that they exert pro-tumorigenic activities (40-42). COL6A1 is a component of triple helical Col6 molecule (α1/α2/α3), L1CAM is a transmembrane protein involved in cell adhesion, and CEMIP is an extracellular matrix protein that binds hyaluronidase and induces hyaluronic acid depolymerization (43-45). By WB analysis, the levels of all three proteins were higher in CM samples from OR cells than DN cells (Fig. 4 B-C), and WB analysis of cell lysates demonstrated a similar pattern for L1CAM and COL6A1 but not CEMIP (Fig. 4 B-C). Based on findings from small interfering RNA (siRNA)-mediated depletion studies, L1CAM, COL6A1, and CEMIP secretion were mediators of Osi resistance (Fig. 4 D-E, Fig. S4 E) and enhanced the proliferative and migratory activities of OR cells (Fig. 4 F-G, Fig. S4 F-I). Treatment of OR cells with Brefeldin A decreased the secretion of L1CAM and COL6A1, whereas treatment with a JAK inhibitor failed to do so (Fig. 4 H, I). These findings suggested that OR cells acquire biologic properties through a secretory program that is SASP-independent.

Conventional secretory pathway activation in OR cells. We sought to elucidate the mechanistic basis for the heightened secretion in OR cells. Fluorescently tagged Rab6A$^+$ secretory vesicles were more numerous in OR cells than DN cells (Fig. S5 A-B) and a fluorescently tagged version of the temperature-sensitive mutant secretory cargo vesicular stomatitis virus-G (VSV-G) was transported from the endoplasmic reticulum to plasma membrane via the Golgi at a faster rate in OR cells than DN cells (Fig. S5 C-D), suggesting that the conventional secretory pathway is activated in OR cells. LC-MS analysis of Golgi-fractionated and vesicular sub-fractionated proteins isolated from H1975-matched DN and OR cells (Fig. S5 E) identified a total of 522 proteins, 271 of which were present at higher levels ($p< 0.05$, > 2-fold change) in OR cells (Fig. S5 F-G), including multiple effectors of the conventional secretory pathway such as RAB GTPases (RAB6C, RAB11B, RAB32) and their associated regulators (RABGEF1, ARHGEF1, ARHGEF2), a molecular motor protein (KIF3b), and a clathrin assembly protein (PICALM). WB analysis of Golgi fractions and vesicle-enriched sub-fractions confirmed these findings (Fig. S5 H). Thus, OR cells and DN cells demonstrated proteomic differences that might underlie heightened secretion in OR cells.

A key regulator of the conventional secretory pathway, the Golgi is composed of flattened membranous cisternae that can disperse or condense and form inter-cisternal, membrane-to-membrane bridges that generate cisternal stacks (46). Cargos diffuse across inter-cisternal bridges and thereby travel from the cis- to the trans-face of the Golgi stack (47). To assess the extent to which the OR cell phenotype is associated with Golgi structural alterations, we quantified Golgi organellar areas and Golgi element numbers and sizes (48), which showed that, compared to DN cells, OR cells generate smaller Golgi in which Golgi elements were larger and fewer in number, indicative of a Golgi compaction process (Fig. 5 A-E). To analyze inter-cisternal connectivity, we performed fluorescence recovery after photobleaching (FRAP) assays using a GFP-tagged Golgi enzyme N-acetylglucosaminyltransferase, which showed that, relative to DN cells, OR cells had faster recovery (Fig. 5 F-H), an indication of greater inter-cisternal connectivity.

EMT drives secretion in OR cells. Golgi compaction, enhanced inter-cisternal connectivity, and heightened secretion are components of an integrated, EMT-driven process (48). OR cells exhibited morphologic and transcriptional evidence of EMT (Fig. 6 A-B, S1 C, S6 A-B), including higher levels of transcriptional drivers of EMT (SNAI1, ZEB1). In The Cancer Genome Atlas LUAD cohort, proteins upregulated in the OR secretome

were correlated with an EMT gene expression signature (Fig. S6 C). Therefore, we reasoned that EMT may be a driver of heightened secretion in OR cells and addressed this possibility by carrying out ZEB1 gain- and loss-of-function studies on DN cells and OR cells, respectively, which showed that ZEB1 enhanced the biogenesis and anterograde transport of secretory vesicles (Fig. 6 C-H, Fig. S6 D-E), increased L1CAM secretion (Fig. 6 I, Fig. S6 F), augmented Osi resistance and mesenchymal features (Fig. S6G-J), and mediated paracrine effects of OR cells on DN cells in mice (Fig. 6 J-L). Thus, EMT underlies heightened secretion in OR cells.

Osi activates TGFβ2 secretion to initiate the EMT-activated secretory pathway. While EMT is a common feature of OR cells (49), the signals that induce EMT in OR cells remain unclear. TGFβ is a potent EMT inducer, and its secretion is reportedly enhanced upon treatment of LUAD cells with an EGFR antagonist (50, 51). In line with this observation, TGFβ2 levels were higher in CM samples from OR cells than DN cells (Fig. 3 A, Fig. 7 A, Fig. S7A). In DN cells, TGFβ2 secretion increased within 4 h of Osi treatment initiation, and the TGFβ2 increase preceded ZEB1 mRNA upregulation (Fig. 7 B-C, Fig. S7B-C). In DN cells, Osi treatment activated a TGFβ2 promoter reporter, and serial deletion studies identified a promoter region that mediated the Osi-induced activation (Fig. 7 D). Treatment of OR cells with anti-TGFβ2 neutralizing antibodies decreased ZEB1 expression (Fig. 7 E, Fig. S7D), dispersed the Golgi (Fig. 7 F, Fig. S7E), and reduced L1CAM secretion (Fig. 7 G, Fig. S7F). In DN cells, treatment with recombinant TGFβ2 increased ZEB1 expression (Fig. 7 H, Fig. S7G), induced Golgi compaction (Fig. 7 I, Fig. S7H) and heightened L1CAM secretion (Fig. 7 J, Fig. S7I). TGFβ2 neutralizing antibodies reversed the effect of Osi on these parameters (Fig. 7 K-L, Fig. S7J-L). In contrast, Ruxolitinib treatment to block SASP had no detectable effect on Golgi areas in OR cells (Fig. S7M). We conclude that TGFβ2 secretion activates an EMT-dependent secretory process that drives biologic properties of OR cells.

Discussion

The “tumor as organizer” model establishes the cancer cell as the primary architect of the tumor microenvironment (21). The cancer cell secretome is comprised of soluble proteins and insoluble vesicles that, through autocrine and paracrine mechanisms, sustain cancer cell survival and recruit various cell types to create an immunosuppressive and fibrotic tumor stroma (52). Continuous exposure to anti-cancer drugs can alter the tumor cell secretome to facilitate drug resistance and disease relapse post-therapy (53-55). Here, we show that Osi treatment of DN cells rapidly activates a heightened secretory state that underlies DTP and OR cell emergence. These findings identify paracrine mechanisms by which OR cells drive LUAD progression.

DTP cells were first identified as bacteria that survive antibiotic treatment through the acquisition of gene mutations (56). In cancer, there is an ongoing debate over whether DTP cells preexist in treatment naïve tumors or evolve from DN cells through induced phenotypic changes (13, 35, 57-59). DTP cells exhibit hallmark features of stem cells, including the capacity to undergo senescence and/or EMT (14, 17, 35, 60). Heightened secretion in DTP cells has been linked to senescence (23, 60), but the findings presented here suggest that senescence is not the sole contributor. We show that Osi induces rapid activation of a TGFβ2/ZEB1-dependent pathway that initiates Golgi remodeling and accelerates the biogenesis and anterograde trafficking of secretory vesicles containing key effectors of the DTP cell phenotype. Thus, we propose that, beyond its established role in promoting Osi resistance in DTP cells (49, 61), EMT activates a secretory program that drives LUAD progression.

DTP-selective therapeutic strategies have been identified that combine Osi with drugs that target unique metabolic features, signaling pathways, or cell surface molecules in DTP cells (17, 49, 62-67). We reported previously that EMT-dependent secretion drives LUAD progression and is therapeutically actionable with selective antagonists of PI4K2A, a Golgi- and endosome-resident enzyme that is upregulated during EMT and drives the biogenesis and trafficking of secretory vesicles and recycling endosomes (25, 68, 69). PI4K2A antagonists are under clinical development for non-oncologic indications (25) and could be repurposed for clinical trials testing their activity against DTP cells in the setting of Osi resistance.

Here we found that Osi activated the secretory program within hours of treatment initiation, suggesting that Osi exerts pro-tumorigenic activity before OR cells emerge. This secretory program could represent a type of non-oncogene addiction (70, 71) if Osi and TGFβ2 inhibition are found to be synthetically lethal in EGFR-mutant LUAD cells. Furthermore, the rapidity with which Osi activated secretion in DN cells raises the possibility that secretory blockade could delay the outgrowth of resistant cells and thereby enhance the therapeutic activity of Osi in drug naïve LUAD patients. This finding could have potential clinical relevance in the front-line treatment setting by utilizing TGFβ antagonists. Indeed, TGFβ2 is a recognized contributor to Osi resistance in LUAD cells and could be targeted with anti-TGFβ2 neutralizing antibodies that are under clinical development (72-74).

Several shortcomings in our study warrant discussion. First, while these findings identify an EMT-activated secretory process that is distinct from SASP, whether the EMT- and senescence-activated secretory programs are activated in overlapping or distinct OR cell populations remains unclear. Indeed, senescence may not be

strictly limited to DTP cells but may also occur in a totally separate population of OR cells (60, 75, 76). Addressing this question has clinical ramifications because senescence is a hallmark on which current efforts to therapeutically target DTP cells is based (77). Second, secretory blockade inhibited certain DTP cell features more prominently than others. For example, proliferation and migration were attenuated to a greater extent than Osi resistance was reversed, suggesting that those features are governed independently. The mechanistic basis for this observation remains unclear. Third, whether the secretory program we identified in cell culture models is operative in patients remains unclear. Elucidating the extent to which TGFβ2 underlies OR in LUAD patients is an important question and must be addressed before TGFβ2 targeting is incorporated into Osi-based therapeutic strategies.

Materials and Methods:

Sex as a biological variable. Our study examined male nu/nu mice because male animals exhibited less variability in phenotype. It is not known whether these findings are relevant for female mice.

Cell lines. Congenic pairs of human EGFR-mutant LUAD cell lines (H1975, HCC827) that are DN or OR were obtained from Dr. John Heymach (UT MD Anderson) and were described previously (49). HCC827_Vec and HCC827_ZEB1 cell lines have been described previously (48) Human LUAD cell lines were cultured in RPMI-1640 supplemented with 10% FBS and were maintained at 37 °C in an incubator with a humidified atmosphere containing 5% CO2. Cells were transfected using XtremeGene 9 DNA Transfection Reagent (Roche) and stable transfectants were selected after 2 weeks following Puromycin treatment. The OR cells were maintained in 10%FBS media with 1μM Osi. Cells were routinely tested for Mycoplasma infections.

Reagents. We purchased fetal bovine serum, RPMI 1640, live-cell imaging solution, PBS, Alexa-fluor tagged secondary antibodies, paraformaldehyde, bovine serum albumin, DAPI, Triton X-100, Lipofectamine RNAiMAX Reagent, Cell-Light Golgi GFP from ThermoFischer scientific; XtremeGene9 DNA transfection reagent from Sigma Millipore; puromycin from InvivoGene; Transwell and Matrigel-coated Boyden chambers from BD Biosciences; collagen-coated glass-bottom dishes and multiwell plates from MatTek; eight-well chamber slides from ThermoFisher scientific; Trypsin from Corning; qScript cDNA super-Mix from Quanta Biosciences; SYBR Green Real-Time PCR Master Mixes from Bimake; Fast Mix from Quanta Biosciences; 10× cell lysis buffer and protease/phosphatase inhibitor cocktail from Cell Signaling Technologies; CCK-8 (#K1018)-6 from APExBIO; Brefeldin A (B7651) from Sigma; Human Recombinant TGFβ-2 protein (100-35B) from Peprotech; DCTN1 (MAB6657-SP) and Anti-TGFβ1,2,3 antibody (MAB1835R-SP) from R&D systems; Osi (#S7297) from Selleckchem; Ruxolitinib (941678-49-5) from Medchem express; RNeasy Plus Mini Kit (#74136) from QIAGEN; siRNAs against human ZEB1 (SASI_Hs01_0011_1599; SASI_Hs01_0011_1598), L1CAM (SASI_Hs01_00084030; SASI_Hs01_00084031), COL6A1 (SASI_Hs01_00014661; SASI_Hs01_00014662), CEMIP(SASI_Hs01_00241050; SASI_Hs01_00241049) and shRNAs against human Rab6A (TRCN0000047985; TRCN0000047987); ZEB1 (TRCN0000017566;TRCN0000017565) and p65 (TRCN0000014683; TRCN0000014686) from Millipore-Sigma; primary antibodies against p-EGFR (8543S), SMAD (8685T), p-SMAD (8828S), Vinculin (4650S), Rab6A (4879S), GM-130 (12480S), β-actin (4970S), p65 (8242T), IL-6 (12153), p-STAT3 (9131S), STAT-3 (9132) from Cell Signaling Technologies; primary antibodies against L1CAM (L4543) from Millipore Sigma; primary antibodies against EGFR (sc-03), COL6A1 (sc-377143), ACBD3 (sc-101277), KIF3B (sc-514165) from Santa Cruz Biotechnology; primary antibodies against CEMIP (21129-1-AP), Myo9B (12432-1-AP), Rabep1 (14350-1-AP), Rabgef1 (12735-1-AP), PICALM (26765) from Proteintech; primary antibodies against VSV-G (#EB0012) from Kerafast; primary antibodies against GEF-H1 (GTX125893) or ZEB1 (GTX105278) from GeneTex; AF568 Phalloidin (A12380) from Thermo Fisher Scientific; wild-type Rab6A-EGFP expression vector (#49469) from Addgene; and adenovirus expressing EGFP-tagged temperature sensitive mutant VSV-G was generously provided by Dr. Anne Muesch (Albert Einstein College of Medicine, New York).

Animal experiments. The nude mice were purchased from The Jackson Laboratory. Mice underwent standard care and were euthanized at predetermined time points or at the first signs of morbidity according to the standards set forth by the Institutional Animal Care and Use Committee. To generate subcutaneous tumors nu/nu mice (n = 5-10 per group) were subcutaneously injected with 1×10^6 human lung cancer cells. To generate orthotopic lung tumors, nu/nu mice were intrathoracically injected with 1×10^6 human LUAD cells containing DN cells alone or in combination with OR cells (10:1 ratio). Primary lung tumors and lung metastases were measured, counted, and confirmed by hematoxylin and eosin staining.

*Vector construction***.** The human TGFβ-2 promoter fragment containing 1837 bp upstream and 137 bp downstream of the transcription start site (TSS) was amplified from genomic DNA of H1299 cells using the primers 5′-TTTCTCTATCGATAGGTACCGAGCTCGTCTATAATGGCCACAGGTGTAAG-3′ and 5′-

AGCTTACTTAGATCGCAGATCTCGAGCCTCTTTCACTTGCGCTCTC-3′. The PCR product was then cloned into the pGL3-Enhancer vector (Promega) using Gibson assembly. Two 5′ truncated TGFβ-2 promoter constructs containing 1078 bp (1.1 kb) and 634 bp (0.6 kb) upstream of the TSS were amplified using the forward primers 5′-ATTTCTCTATCGATAGGTACCGAGCTCAGGCCCCATACACAACTGAA-3′ and 5′-ATTTCTCTATCGATAGGTACCGAGCTCGCAGCAAATTATAAAGGTGACCATTC-3′, respectively.

EGFR sequencing. Exons 18 to 21 of the human EGFR gene were amplified from cDNAs synthesized from parental and Osi-resistant H1975 and HCC827 cells using the primers 5′-ATCGGCCTCTTCATGCGAAG-3′ and 5′-CGTAGCTCCAGACATCACTCTG-3′. The purified PCR products were subsequently submitted for Sanger sequencing to examine hotspot mutations in EGFR.

LC-MS analysis. To identify differentially secreted proteins, we collected and concentrated CM Samples from DN cells and OR cells using Amicon® Ultra Centrifugal Filters (Sigma) and subjected them to LC-MS as previously described (69). To identify proteins in the Golgi and vesicle enriched subfractions, the fractions were isolated following manufacturer's protocol and the samples were subjected to LC-MS analysis.

Isolation of Golgi- and vesicle-enriched subcellular fractions. As previously described (28), the Minute Golgi Apparatus Enrichment Kit (GO-037, Invent Biotechnologies) was used to enrich cell lysates in Golgi and vesicle fractions, following the manufacturer's instructions.

Cell Proliferation and Dose Response Assays. Cells were seeded on 96-well plates at a density of 2000 cells per well and incubated overnight. For Dose Response Assays, medium was replaced on the following day with 10%FBS containing RPMI and various concentrations of Osi (0-10 μM), and cells were allowed to proliferate for 72 h. Relative cell density was measured by using the CCK-8 Counting Kit according to the manufacturer's instructions. Briefly, cells were incubated with culture medium containing the CCK-8 solution for 2 h at 37 °C, and the absorbance was read at 450 nm.

Cell Migration and Invasion Assays. As described previously (48), 1×10^5 cells were seeded in the upper wells of Transwell plates (BD Biosciences) for migration assays or Matrigel-coated Boyden chambers (BDBiosciences) for invasion assays. Cells were allowed to migrate toward 10% FBS in the bottom wells. After 16 h of incubation, migrating or invading cells were stained with 0.1% crystal violet, photographed and counted.

VSV-G Assay. The VSV-G transport assay was performed as described previously (48, 69). In brief, cells were infected with adenovirus expressing EGFP-VSV-G (ts045). The cells were then transferred to the restrictive temperature of 40 °C for 20 h and transferred to the permissive temperature of 32 °C for 1 h in the presence of 100 mg/mL cycloheximide and then the cells were fixed. In non-permeabilized cells, exofacial and total VSV-G were detected by staining with an anti-VSV-G antibody and by measurement of EGFP signal intensity, respectively. VSV- G trafficking to the plasma membrane was measured based on the ratio of exofacial (surface) VSV-G fluorescence signal to the EGFP (total) signal intensity.

CM transfer assay. $2x10^6$ cells were plated in 10-cm dishes and incubated overnight. The cells were serum-starved for 16 h and the supernatants (CM) were collected, filtered through a 0.45-μm filter, mixed with complete growth medium (1:1) and added to cells. Cells were pre-treated with respective CM samples for 3 days following which the cells were trypsinized and plated for further assays.

β-galactosidase staining assay. Cells were plated in 35 mm-dishes and following pre-determined treatments, the β-galactosidase staining assay was performed using the senescence β-galactosidase staining kit (#9860; Cell Signaling Technologies) according to manufacturer's instructions. Briefly, cells were fixed in fixation solution for 10 min at RT, β-galactosidase staining solution was added and cells were incubated overnight. Stained cells were imaged and counted.

Immunology Multiplex Assay. As described previously (69) CM samples were collected, prepared and analyzed using a multiplex magnetic bead-based assay (HCYTA-60K MILLIPLEX Human Cytokine/Chemokine/Growth Factor Panel A; Luminex 200 System, Luminex and Multiplex Analysis 5.1 software, Millipore-Sigma) to quantify cytokine concentrations in CM samples.

WB analysis. Cells were cultured up to 80% confluency, washed three times with PBS and harvested with 1x Cell lysis buffer. The supernatant was mixed with 2× Laemmli buffer (Bio-Rad). The cell lysate was boiled for 10 min and loaded onto an SDS gel. After transferring to a nitrocellulose membrane (Bio-Rad), membranes were blocked with 5% milk in PBST buffer and were probed with primary antibodies diluted in 5% BSA or milk in PBST buffer. Horseradish peroxidase-conjugated secondary antibodies were used for detection according to the manufacturer's instructions and images were obtained using Chemidoc Imaging System (BioRad) and quantified using ImageJ (78).

Quantitative PCR analysis. The RNeasy Mini Kit (Qiagen, 74106) was used to isolate total RNA which was reverse transcribed using the qScript cDNA superMix (Quanta Biosciences). The mRNA levels were determined

using SYBR Green Real-Time PCR Master Mixes (21203, Bimake) and normalized to ribosomal protein L32 mRNA (RL32, for mRNAs). PCR primers utilized are listed (Table S1).

Dual-luciferase reporter assay. TGFβ-2 promoter luciferase reporter plasmids (800 ng) and pRL-TK (200 ng) were co-transfected into HCC827 DN cells. After 48 hours, cells were treated with DMSO or Osi for an additional 24 hours. Luciferase activity was then measured using the Dual-Luciferase Reporter Assay System (Promega), according to the manufacturer's instructions.

Fixed Cell Imaging. Cells were seeded on type I collagen-coated cover glass (#1.5) and were fixed using 4% paraformaldehyde for 10 min, permeabilized using 0.1% Triton X-100 for 5 min and blocked with 5% BSA for 30 min. Overnight incubation was performed primary antibody diluted in blocking buffer at 4 °C. Following this, the cells were incubated in Alexa Fluor–conjugated secondary antibodies (1:500) in blocking buffer for 1 h at RT. Nuclei were counterstained and mounted with Prolong Gold Anti-Fade Mountant with DAPI (P35941, Invitrogen). PBS washing was done 3 times after each step and was also used as the solvent in all steps. For surface exposure of VSV-G assay, the cells were not permeabilized.

Rab6A+ vesicle imaging and quantification. The Rab6A$^+$ vesicle imaging was performed by overexpressing wild-type Rab6A-EGFP expression vector (Addgene). The number of EGFP-Rab6A$^+$ vesicles were determined from maximum intensity projections of deconvolved, thresholded (Otsu) and watershed-segmented 3D stacks by particle analysis using ImageJ.

Golgi structural analysis. The area occupied by GM130-stained structures was quantified in volume projections with a limiting polygon as described previously (79). The Golgi area was divided by the nucleus area in the same cell to generate a normalized area fraction. Cells were chosen randomly for such measurements. Golgi element size and number were determined from maximum intensity projections of deconvolved, thresholded (Otsu) and watershed-segmented 3D stacks by particle analysis using ImageJ.

Image Acquisition and Quantification. Confocal imaging was performed on an A1+ platform (Nikon Instruments) equipped with 63X/1.4 NA Oil, 100X/1.45 NA Oil and 20X/0.75 NA Air objectives; 405/488/561 nm laser lines and images were acquired using NIS-Elements software (Nikon instruments). Routine wide-field fluorescence, bright field and phase-contrast imaging were performed on an IX71 microscope (Olympus). The images were processed and fluorescent intensity was analyzed in Fiji/ImageJ. The Golgi organelle area and Golgi element numbers were quantified in volume projections with a limiting polygon through the area occupied by GM130-stained structures as described previously (48).

FRAP assays. Cells were cultured overnight in poly-L-lysine-coated 8-well chamber slides (#1.5,155409, Lab-Tek) and Golgi was stained with Cell Light Golgi-GFP BacMam 2.0 overnight (C10592, ThermoFisher). FRAP assays were performed as described previously (48) with some modifications. In brief, the recovery was calculated in a circular region of interest of 1uM diameter. Ten pre-bleach images were acquired and averaged to obtain an estimated prebleach intensity. Laser power was adjusted to get ~80% bleach depth in 2 iterations. Post-bleach images were acquired with no delay to record the diffusion component phase and then at 10 second intervals to record the binding component phase. The fluorescence recovery was calculated as mentioned previously (79).

Immunohistochemistry. 4 μm tissue sections from formalin-fixed and paraffin-embedded lung tumor tissues were stained using an automated immune-stainer platform, the Leica Bond Max automated stainer (Leica Biosystems Nussloch GmbH). Following the Leica Bond protocol, the tissue sections were deparaffinized and rehydrated. Slides were counterstained with hematoxylin, dehydrated and cover slipped. H&E-stained sections were digitally scanned using the Aperio AT2 slide scanner (Leica Biosystems) under 20 × objective magnification.

Statistics. Unless stated otherwise, the results shown are representative of replicated experiments and data represent the mean ± SD from triplicate samples or randomly chosen cells within a field. When comparing EMT scores in human lung cancers the EMT score was calculated as previously described (80). Kaplan-Meier survival data were generated using KMPlot (81). Statistical evaluations were carried out with Prism 10 (GraphPad Software, Inc.). Unpaired two-tailed Student t-tests were used to compare the means of two groups and ANOVA with Dunnett's test was used to compare multiple groups to a control. p-values < 0.05 were considered statistically significant.

Study Approval. All mouse studies were approved by the Institutional Animal Care and Use Committee at The University of Texas MD Anderson Cancer Center (Houston, Texas).

Data availability. All data associated with this study are present in the manuscript or in the supplemental figures, tables, and supporting data values file.

Author contributions

JMK and MG wrote the paper. MG conceived, designed, executed, and interpreted the molecular biology, cell biology and in vivo experiments. CW conceived, designed and executed cloning the TGFβ-2 promoter, EGFR sequencing, and assisted MG with Western blot experiments. MN and JVH conceived, designed and executed the generation of OR-cells. ND assisted MG with the Rab6A+ vesicle imaging and quantification. AK assisted MG with the FRAP assay and β-galactosidase staining assays and Golgi area quantification. WG and XL assisted MG with the in vivo experiments. JY bred the mice for the in vivo studies. GX assisted MG with the VSV-G assay. AC assisted MG with recombinant and neutralizing TGF-β2 experiments. KG assisted MG with Golgi fractionation and vesicle sub-fractionation studies. WKR directed and interpreted the LC-MS experiments. C.J.C generated TCGA LUAD cohort EMT-gene signature data. SW conducted quantitative PCR analysis on EMT markers. XT assisted MG with the design, execution, and interpretation of the molecular and cell biology experiments, as well as the manuscript revision. JMK conceived and supervised the project and contributed to the design and interpretation of all experiments.

Acknowledgments
This work was supported in part by grants from the NIH (R01CA236781 and R01CA255021-01 to JMK, 5R50CA265307 to MN, R01CA280382 to XT). The UTMB Mass Spectrometry Facility is supported in part by CPRIT grant RP190682 (to WKR). JMK holds the Gloria Lupton Tennison Distinguished Professorship in Lung Cancer.

Address correspondence to: Jonathan M. Kurie, Department of Thoracic/Head and Neck Medical Oncology, Box 432, MD Anderson Cancer Center, 1515 Holcombe Blvd, Houston, Texas 77030, USA. Email: jkurie@mdanderson.org. Or to: Xiaochao Tan, Section of Hematology and Oncology, Department of Medicine, Tulane University School of Medicine, New Orleans, Louisiana 70112, USA.; Email: xtan4@tulane.edu.

Conflict of Interest: The authors have declared that no conflict of interest exists.

References

1. Weinstein IB. Cancer. Addiction to oncogenes--the Achilles heal of cancer. *Science*. 2002;297(5578):63-4.
2. Weinstein IB, and Joe AK. Mechanisms of disease: Oncogene addiction--a rationale for molecular targeting in cancer therapy. *Nat Clin Pract Oncol*. 2006;3(8):448-57.
3. Cancer Genome Atlas Research N. Comprehensive molecular profiling of lung adenocarcinoma. *Nature*. 2014;511(7511):543-50.
4. Zhou YZ, Wang Q, Xie LX, and Lu S. Analysis of In Situ Fluorescent Probes for Rapid Screening of Epidermal Growth Factor Receptor and KRAS Mutations in Exfoliated Cells from Pleural Fluid in Patients with Lung Cancer. *J Biomed Nanotechnol*. 2023;19(10):1738-45.
5. Rosell R, Moran T, Queralt C, Porta R, Cardenal F, Camps C, et al. Screening for Epidermal Growth Factor Receptor Mutations in Lung Cancer. *New Engl J Med*. 2009;361(10):958-U38.
6. Remon J, Steuer CE, Ramalingam SS, and Felip E. Osimertinib and other third-generation EGFR TKI in EGFR-mutant NSCLC patients. *Ann Oncol*. 2018;29(suppl_1):i20-i7.
7. Mok TS, Wu YL, Thongprasert S, Yang CH, Chu DT, Saijo N, et al. Gefitinib or carboplatin-paclitaxel in pulmonary adenocarcinoma. *N Engl J Med*. 2009;361(10):947-57.
8. Mok TS, Wu YL, Ahn MJ, Garassino MC, Kim HR, Ramalingam SS, et al. Osimertinib or Platinum-Pemetrexed in EGFR T790M-Positive Lung Cancer. *N Engl J Med*. 2017;376(7):629-40.
9. Cross DA, Ashton SE, Ghiorghiu S, Eberlein C, Nebhan CA, Spitzler PJ, et al. AZD9291, an irreversible EGFR TKI, overcomes T790M-mediated resistance to EGFR inhibitors in lung cancer. *Cancer Discov*. 2014;4(9):1046-61.
10. John T, Akamatsu H, Delmonte A, Su WC, Lee JS, Chang GC, et al. EGFR mutation analysis for prospective patient selection in AURA3 phase III trial of osimertinib versus platinum-pemetrexed in patients with EGFR T790M-positive advanced non-small-cell lung cancer. *Lung Cancer*. 2018;126:133-8.
11. Soria JC, Ohe Y, Vansteenkiste J, Reungwetwattana T, Chewaskulyong B, Lee KH, et al. Osimertinib in Untreated EGFR-Mutated Advanced Non-Small-Cell Lung Cancer. *N Engl J Med*. 2018;378(2):113-25.
12. Kurppa KJ, Liu Y, To C, Zhang TH, Fan MY, Vajdi A, et al. Treatment-Induced Tumor Dormancy through YAP-Mediated Transcriptional Reprogramming of the Apoptotic Pathway. *Cancer Cell*. 2020;37(1):104-+.

13. Echeverria GV, Ge Z, Seth S, Zhang X, Jeter-Jones S, Zhou X, et al. Resistance to neoadjuvant chemotherapy in triple-negative breast cancer mediated by a reversible drug-tolerant state. *Sci Transl Med*. 2019;11(488).
14. Arasada RR, Amann JM, Rahman MA, Huppert SS, and Carbone DP. EGFR blockade enriches for lung cancer stem-like cells through Notch3-dependent signaling. *Cancer Res*. 2014;74(19):5572-84.
15. Chen J, Li Y, Yu TS, McKay RM, Burns DK, Kernie SG, et al. A restricted cell population propagates glioblastoma growth after chemotherapy. *Nature*. 2012;488(7412):522-6.
16. Aldonza MBD, Ku J, Hong JY, Kim D, Yu SJ, Lee MS, et al. Prior acquired resistance to paclitaxel relays diverse EGFR-targeted therapy persistence mechanisms. *Sci Adv*. 2020;6(6):eaav7416.
17. Raoof S, Mulford IJ, Frisco-Cabanos H, Nangia V, Timonina D, Labrot E, et al. Targeting FGFR overcomes EMT-mediated resistance in EGFR mutant non-small cell lung cancer. *Oncogene*. 2019;38(37):6399-413.
18. Dannenberg JH, and Berns A. Drugging drug resistance. *Cell*. 2010;141(1):18-20.
19. Guler GD, Tindell CA, Pitti R, Wilson C, Nichols K, KaiWai Cheung T, et al. Repression of Stress-Induced LINE-1 Expression Protects Cancer Cell Subpopulations from Lethal Drug Exposure. *Cancer Cell*. 2017;32(2):221-37 e13.
20. Sharma SV, Lee DY, Li B, Quinlan MP, Takahashi F, Maheswaran S, et al. A chromatin-mediated reversible drug-tolerant state in cancer cell subpopulations. *Cell*. 2010;141(1):69-80.
21. Li J, and Stanger BZ. The tumor as organizer model. *Science*. 2019;363(6431):1038-9.
22. Madden EC, Gorman AM, Logue SE, and Samali A. Tumour Cell Secretome in Chemoresistance and Tumour Recurrence. *Trends Cancer*. 2020;6(6):489-505.
23. Patel SA, Nilsson MB, Yang Y, Le X, Tran HT, Elamin YY, et al. IL6 Mediates Suppression of T- and NK-cell Function in EMT-associated TKI-resistant EGFR-mutant NSCLC. *Clin Cancer Res*. 2023;29(7):1292-304.
24. Xiao GY, Tan X, Rodriguez BL, Gibbons DL, Wang S, Wu C, et al. EMT activates exocytotic Rabs to coordinate invasion and immunosuppression in lung cancer. *Proc Natl Acad Sci U S A*. 2023;120(28):e2220276120.
25. Tan X, Xiao GY, Wang S, Shi L, Zhao Y, Liu X, et al. EMT-activated secretory and endocytic vesicular trafficking programs underlie a vulnerability to PI4K2A antagonism in lung cancer. *J Clin Invest*. 2023;133(7).
26. Yadav S, and Linstedt AD. Golgi Positioning. *Csh Perspect Biol*. 2011;3(5).
27. Tan X, Banerjee P, Shi L, Xiao GY, Rodriguez BL, Grzeskowiak CL, et al. p53 loss activates prometastatic secretory vesicle biogenesis in the Golgi. *Sci Adv*. 2021;7(25).
28. Tan X, Shi L, Banerjee P, Liu X, Guo HF, Yu J, et al. A protumorigenic secretory pathway activated by p53 deficiency in lung adenocarcinoma. *J Clin Invest*. 2021;131(1).
29. Tan XC, Wang SK, Xiao GY, Wu C, Liu X, Zhou BY, et al. Chromosomal 3q amplicon encodes essential regulators of secretory vesicles that drive secretory addiction in cancer. *J Clin Invest*. 2024;134(12).
30. Chien Y, Scuoppo C, Wang X, Fang X, Balgley B, Bolden JE, et al. Control of the senescence-associated secretory phenotype by NF-kappaB promotes senescence and enhances chemosensitivity. *Genes Dev*. 2011;25(20):2125-36.
31. Orjalo AV, Bhaumik D, Gengler BK, Scott GK, and Campisi J. Cell surface-bound IL-1alpha is an upstream regulator of the senescence-associated IL-6/IL-8 cytokine network. *Proc Natl Acad Sci U S A*. 2009;106(40):17031-6.
32. Meraz IM, Majidi M, Fang B, Meng F, Gao L, Shao R, et al. 3-Phosphoinositide-dependent kinase 1 drives acquired resistance to osimertinib. *Commun Biol*. 2023;6(1):509.
33. Grigoriev I, Yu KL, Martinez-Sanchez E, Serra-Marques A, Smal I, Meijering E, et al. Rab6, Rab8, and MICAL3 cooperate in controlling docking and fusion of exocytotic carriers. *Curr Biol*. 2011;21(11):967-74.
34. Nebenfuhr A, Ritzenthaler C, and Robinson DG. Brefeldin A: deciphering an enigmatic inhibitor of secretion. *Plant Physiol*. 2002;130(3):1102-8.
35. Rehman SK, Haynes J, Collignon E, Brown KR, Wang Y, Nixon AML, et al. Colorectal Cancer Cells Enter a Diapause-like DTP State to Survive Chemotherapy. *Cell*. 2021;184(1):226-42 e21.
36. Ibusuki R, Iwama E, Shimauchi A, Tsutsumi H, Yoneshima Y, Tanaka K, et al. TP53 gain-of-function mutations promote osimertinib resistance via TNF-alpha-NF-kappaB signaling in EGFR-mutated lung cancer. *NPJ Precis Oncol*. 2024;8(1):60.
37. Wang Y, Zhou Q, Liu C, Zhang R, Xing B, Du J, et al. Targeting IL-6/STAT3 signaling abrogates EGFR-TKI resistance through inhibiting Beclin-1 dependent autophagy in HNSCC. *Cancer Lett*. 2024;586:216612.
38. Wang J, Jacob NK, Ladner KJ, Beg A, Perko JD, Tanner SM, et al. RelA/p65 functions to maintain cellular senescence by regulating genomic stability and DNA repair. *EMBO Rep*. 2009;10(11):1272-8.

39. Xu M, Tchkonia T, Ding H, Ogrodnik M, Lubbers ER, Pirtskhalava T, et al. JAK inhibition alleviates the cellular senescence-associated secretory phenotype and frailty in old age. *Proc Natl Acad Sci U S A*. 2015;112(46):E6301-10.
40. Owusu-Ansah KG, Song G, Chen R, Edoo MIA, Li J, Chen B, et al. COL6A1 promotes metastasis and predicts poor prognosis in patients with pancreatic cancer. *Int J Oncol*. 2019;55(2):391-404.
41. Ganesh K, Basnet H, Kaygusuz Y, Laughney AM, He L, Sharma R, et al. L1CAM defines the regenerative origin of metastasis-initiating cells in colorectal cancer. *Nat Cancer*. 2020;1(1):28-45.
42. Rodrigues G, Hoshino A, Kenific CM, Matei IR, Steiner L, Freitas D, et al. Tumour exosomal CEMIP protein promotes cancer cell colonization in brain metastasis. *Nat Cell Biol*. 2019;21(11):1403-12.
43. Brummendorf T, Kenwrick S, and Rathjen FG. Neural cell recognition molecule L1: from cell biology to human hereditary brain malformations. *Curr Opin Neurobiol*. 1998;8(1):87-97.
44. Yoshida H, Nagaoka A, Kusaka-Kikushima A, Tobiishi M, Kawabata K, Sayo T, et al. KIAA1199, a deafness gene of unknown function, is a new hyaluronan binding protein involved in hyaluronan depolymerization. *Proc Natl Acad Sci U S A*. 2013;110(14):5612-7.
45. Chu ML, Pan TC, Conway D, Kuo HJ, Glanville RW, Timpl R, et al. Sequence analysis of alpha 1(VI) and alpha 2(VI) chains of human type VI collagen reveals internal triplication of globular domains similar to the A domains of von Willebrand factor and two alpha 2(VI) chain variants that differ in the carboxy terminus. *EMBO J*. 1989;8(7):1939-46.
46. Ladinsky MS, Mastronarde DN, McIntosh JR, Howell KE, and Staehelin LA. Golgi structure in three dimensions: functional insights from the normal rat kidney cell. *J Cell Biol*. 1999;144(6):1135-49.
47. Dippold HC, Ng MM, Farber-Katz SE, Lee SK, Kerr ML, Peterman MC, et al. GOLPH3 bridges phosphatidylinositol-4- phosphate and actomyosin to stretch and shape the Golgi to promote budding. *Cell*. 2009;139(2):337-51.
48. Tan X, Banerjee P, Guo HF, Ireland S, Pankova D, Ahn YH, et al. Epithelial-to-mesenchymal transition drives a pro-metastatic Golgi compaction process through scaffolding protein PAQR11. *J Clin Invest*. 2017;127(1):117-31.
49. Nilsson MB, Sun H, Robichaux J, Pfeifer M, McDermott U, Travers J, et al. A YAP/FOXM1 axis mediates EMT-associated EGFR inhibitor resistance and increased expression of spindle assembly checkpoint components. *Sci Transl Med*. 2020;12(559).
50. Soucheray M, Capelletti M, Pulido I, Kuang Y, Paweletz CP, Becker JH, et al. Intratumoral Heterogeneity in EGFR-Mutant NSCLC Results in Divergent Resistance Mechanisms in Response to EGFR Tyrosine Kinase Inhibition. *Cancer Res*. 2015;75(20):4372-83.
51. Yao Z, Fenoglio S, Gao DC, Camiolo M, Stiles B, Lindsted T, et al. TGF-beta IL-6 axis mediates selective and adaptive mechanisms of resistance to molecular targeted therapy in lung cancer. *Proc Natl Acad Sci U S A*. 2010;107(35):15535-40.
52. Ritchie S, Reed DA, Pereira BA, and Timpson P. The cancer cell secretome drives cooperative manipulation of the tumour microenvironment to accelerate tumourigenesis. *Fac Rev*. 2021;10:4.
53. Demaria M, O'Leary MN, Chang J, Shao L, Liu S, Alimirah F, et al. Cellular Senescence Promotes Adverse Effects of Chemotherapy and Cancer Relapse. *Cancer Discov*. 2017;7(2):165-76.
54. Mastri M, Tracz A, Lee CR, Dolan M, Attwood K, Christensen JG, et al. A Transient Pseudosenescent Secretome Promotes Tumor Growth after Antiangiogenic Therapy Withdrawal. *Cell Rep*. 2018;25(13):3706-20 e8.
55. Madden EC, Gorman AM, Logue SE, and Samali A. Tumour Cell Secretome in Chemoresistance and Tumour Recurrence. *Trends Cancer*. 2020;6(6):489-505.
56. Fisher RA, Gollan B, and Helaine S. Persistent bacterial infections and persister cells. *Nat Rev Microbiol*. 2017;15(8):453-64.
57. Dagogo-Jack I, and Shaw AT. Tumour heterogeneity and resistance to cancer therapies. *Nat Rev Clin Oncol*. 2018;15(2):81-94.
58. McNeer NA, Philip J, Geiger H, Ries RE, Lavallee VP, Walsh M, et al. Genetic mechanisms of primary chemotherapy resistance in pediatric acute myeloid leukemia. *Leukemia*. 2019;33(8):1934-43.
59. Shaffer SM, Dunagin MC, Torborg SR, Torre EA, Emert B, Krepler C, et al. Rare cell variability and drug-induced reprogramming as a mode of cancer drug resistance. *Nature*. 2017;546(7658):431-5.

60. Kurppa KJ, Liu Y, To C, Zhang T, Fan M, Vajdi A, et al. Treatment-Induced Tumor Dormancy through YAP-Mediated Transcriptional Reprogramming of the Apoptotic Pathway. *Cancer Cell*. 2020;37(1):104-22 e12.
61. Nilsson MB, Yang Y, Heeke S, Patel SA, Poteete A, Udagawa H, et al. CD70 is a therapeutic target upregulated in EMT-associated EGFR tyrosine kinase inhibitor resistance. *Cancer Cell*. 2023;41(2):340-55 e6.
62. Lotsberg ML, Wnuk-Lipinska K, Terry S, Tan TZ, Lu N, Trachsel-Moncho L, et al. AXL Targeting Abrogates Autophagic Flux and Induces Immunogenic Cell Death in Drug-Resistant Cancer Cells. *J Thorac Oncol*. 2020;15(6):973-99.
63. Le X, Puri S, Negrao MV, Nilsson MB, Robichaux J, Boyle T, et al. Landscape of EGFR-Dependent and -Independent Resistance Mechanisms to Osimertinib and Continuation Therapy Beyond Progression in EGFR-Mutant NSCLC. *Clin Cancer Res*. 2018;24(24):6195-203.
64. Janne PA, Baik C, Su WC, Johnson ML, Hayashi H, Nishio M, et al. Efficacy and Safety of Patritumab Deruxtecan (HER3-DXd) in EGFR Inhibitor-Resistant, EGFR-Mutated Non-Small Cell Lung Cancer. *Cancer Discov*. 2022;12(1):74-89.
65. Wang R, Yamada T, Kita K, Taniguchi H, Arai S, Fukuda K, et al. Transient IGF-1R inhibition combined with osimertinib eradicates AXL-low expressing EGFR mutated lung cancer. *Nat Commun*. 2020;11(1):4607.
66. Cho BC, Simi A, Sabari J, Vijayaraghavan S, Moores S, and Spira A. Amivantamab, an Epidermal Growth Factor Receptor (EGFR) and Mesenchymal-epithelial Transition Factor (MET) Bispecific Antibody, Designed to Enable Multiple Mechanisms of Action and Broad Clinical Applications. *Clin Lung Cancer*. 2023;24(2):89-97.
67. Kurppa KJ, Liu Y, To C, Zhang T, Fan M, Vajdi A, et al. Treatment-Induced Tumor Dormancy through YAP-Mediated Transcriptional Reprogramming of the Apoptotic Pathway. *Cancer Cell*. 2020;37(1):104-22 e12.
68. Shi Y, McKenery A, Dolan M, Mastri M, Hill JW, Dommer A, et al. Acquired resistance to PD-L1 inhibition enhances a type I IFN-regulated secretory program in tumors. *EMBO Rep*. 2025;26(2):521-59.
69. Tan X, Banerjee P, Pham EA, Rutaganira FUN, Basu K, Bota-Rabassedas N, et al. PI4KIIIbeta is a therapeutic target in chromosome 1q-amplified lung adenocarcinoma. *Sci Transl Med*. 2020;12(527).
70. Muller AJ, and Scherle PA. Targeting the mechanisms of tumoral immune tolerance with small-molecule inhibitors. *Nat Rev Cancer*. 2006;6(8):613-25.
71. Luo J, Solimini NL, and Elledge SJ. Principles of cancer therapy: oncogene and non-oncogene addiction. *Cell*. 2009;136(5):823-37.
72. Jiang XM, Xu YL, Yuan LW, Zhang LL, Huang MY, Ye ZH, et al. TGFbeta2-mediated epithelial-mesenchymal transition and NF-kappaB pathway activation contribute to osimertinib resistance. *Acta Pharmacol Sin*. 2021;42(3):451-9.
73. Bauer TM, Santoro A, Lin CC, Garrido-Laguna I, Joerger M, Greil R, et al. Phase I/Ib, open-label, multicenter, dose-escalation study of the anti-TGF-beta monoclonal antibody, NIS793, in combination with spartalizumab in adult patients with advanced tumors. *J Immunother Cancer*. 2023;11(11).
74. Kim BG, Malek E, Choi SH, Ignatz-Hoover JJ, and Driscoll JJ. Novel therapies emerging in oncology to target the TGF-beta pathway. *J Hematol Oncol*. 2021;14(1):55.
75. Mani SA, Guo W, Liao MJ, Eaton EN, Ayyanan A, Zhou AY, et al. The epithelial-mesenchymal transition generates cells with properties of stem cells. *Cell*. 2008;133(4):704-15.
76. Hinohara K, and Polyak K. Intratumoral Heterogeneity: More Than Just Mutations. *Trends Cell Biol*. 2019;29(7):569-79.
77. Wang L, Lankhorst L, and Bernards R. Exploiting senescence for the treatment of cancer. *Nat Rev Cancer*. 2022;22(6):340-55.
78. Schindelin J, Arganda-Carreras I, Frise E, Kaynig V, Longair M, Pietzsch T, et al. Fiji: an open-source platform for biological-image analysis. *Nat Methods*. 2012;9(7):676-82.
79. Banerjee P, Tan X, Russell WK, and Kurie JM. Analysis of Golgi Secretory Functions in Cancer. *Methods Mol Biol*. 2023;2557:785-810.
80. Byers LA, Diao L, Wang J, Saintigny P, Girard L, Peyton M, et al. An epithelial-mesenchymal transition gene signature predicts resistance to EGFR and PI3K inhibitors and identifies Axl as a therapeutic target for overcoming EGFR inhibitor resistance. *Clin Cancer Res*. 2013;19(1):279-90.
81. Nagy A, Munkacsy G, and Gyorffy B. Pancancer survival analysis of cancer hallmark genes. *Sci Rep*. 2021;11(1):6047.

Figures and legends

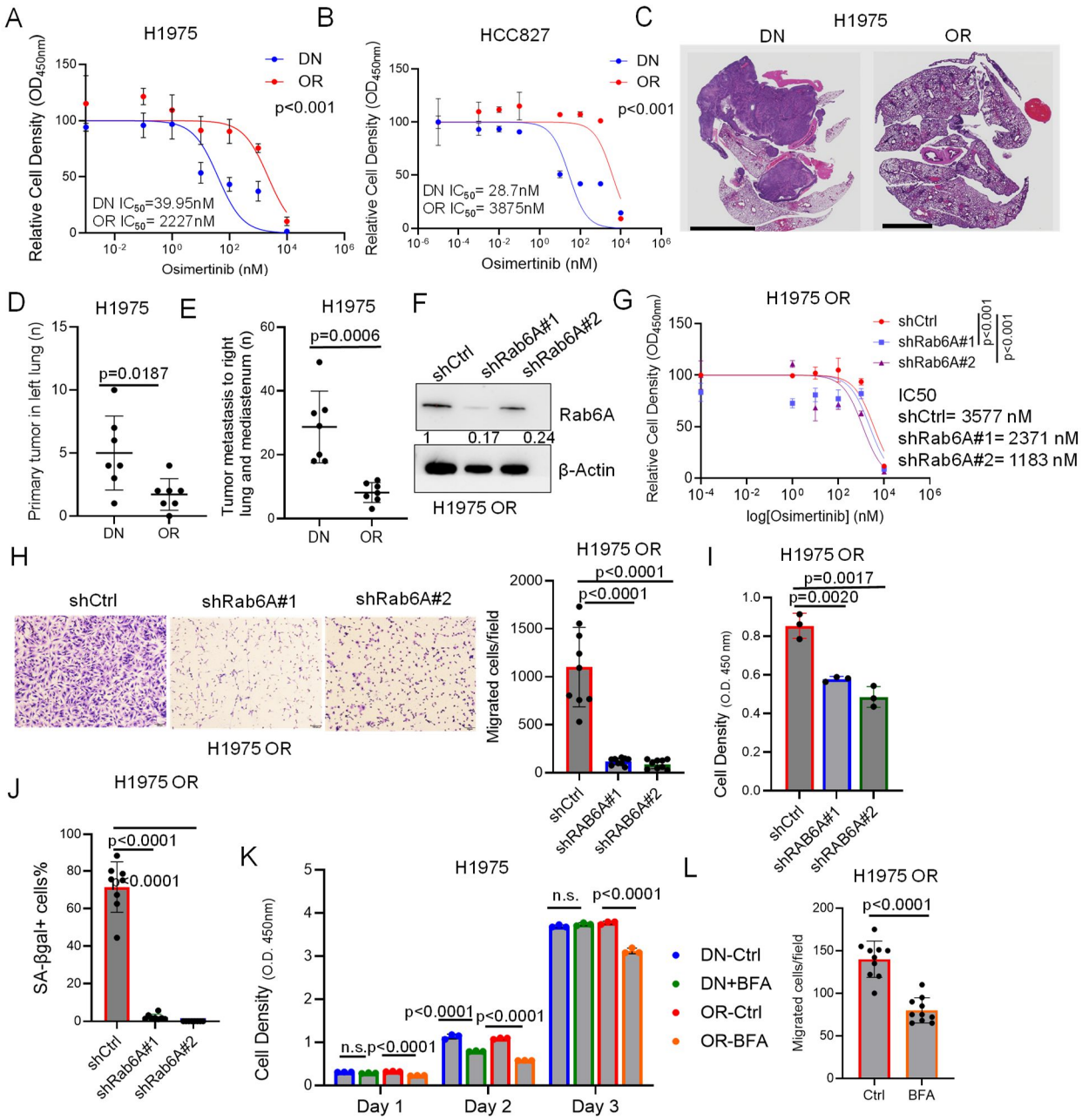

Figure 1. Secretory processes drive biological differences between drug-naïve (DN) and OR LUAD cells. (A, B) Relative densities of H1975 cells (A) and HCC827 cells (B) (OR and DN) following 3 days of Osi treatment in monolayer culture. Results expressed relative to DMSO control. IC50 values (bottom) were calculated. (C-E) Histology of orthotopic lung tumor sections; scale bars, 5mm (C). H1975 cells (OR or DN) were injected intrathoracically into nu/nu mice to grow lung tumors for 6 weeks. At necropsy, each mouse (dot) was scored based on primary lung tumor numbers (D) and mediastinal lymph node and contralateral lung tumor metastases (E). (F) WB confirmation of target gene depletion in short hairpin RNA (shRNA)-transfected H1975 OR cells. Densitometric values expressed relative to shCtrl. β-actin loading control. (G) Relative densities of shRNA-transfected H1975 OR cells treated with Osimertinib in monolayer culture. IC50 values (right) were calculated. (H) Boyden chamber migration assays. Scale bars 100• m. Results expressed as an average number of migrated cells per field (bar graph). (I) Densities of shRNA-transfected cells in monolayer culture. (J) SA β-galactosidase staining assay on shRNA-transfected cells. Results expressed as a percentage of β-galactosidase+ cells per field. (K) Densities of H1975 cells (OR or DN) in monolayer culture. Cells were pre-treated for 4 h with 10ug/ml brefeldin A (BFA) and quantified daily for 3 days. (L) Boyden chamber migration assays. Cells were pre-treated for 4 h with 10 ug/ml BFA and seeded into chambers. Migrated cells were visualized and quantified 18 h after seeding. Results expressed as an average number of migrated cells per

field. Data are the mean ± SD from a single experiment incorporating biological replicate samples (n = 3, unless otherwise indicated) and are representative of at least 2 independent experiments. Two-way ANOVA test (A, B, and G). Two-tailed Student's t test (D, E, and L). One-way ANOVA test (H-K).

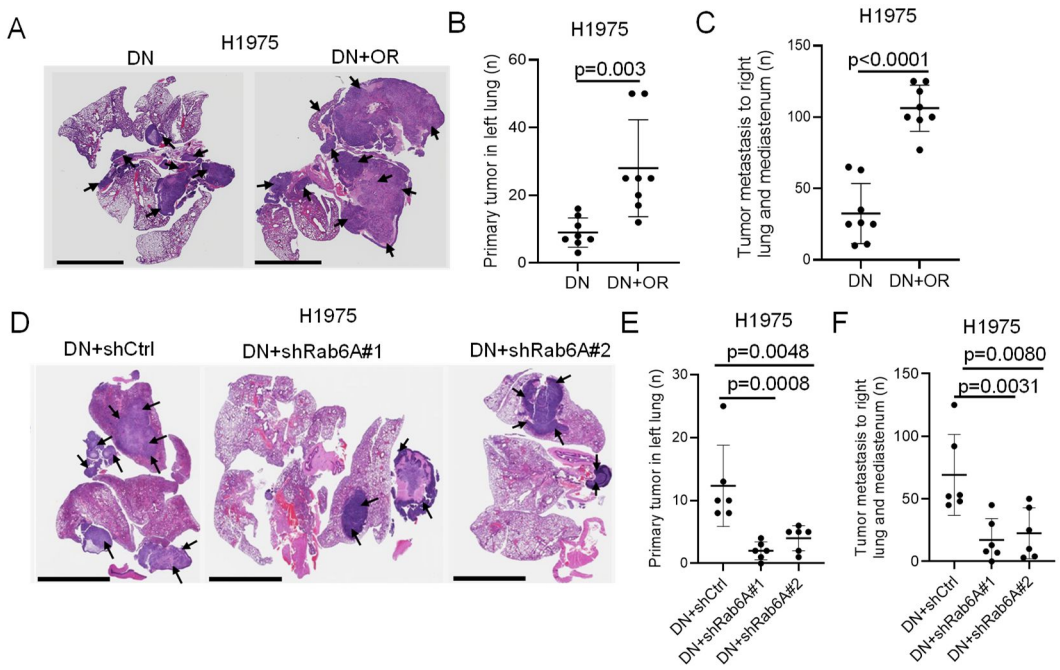

Figure 2. OR cells exert paracrine effects on DN cells in tumor models. (A-C) Histology of orthotopic lung tumor sections; scale bars, 5mm (A). DN cells were intrathoracically injected alone (DN) or in combination with OR cells (DN+OR, 10:1 ratio) into nu/nu mice to grow tumors for 4 weeks. At necropsy, each mouse (dot) was scored as described above (B, C). (D-F) Histology of orthotopic lung tumor sections; scale bars, 5mm (D). DN cells were injected alone or in combination with either Rab6A-replete (shCtrl) or -deficient (shRab6A#1 or #2) OR cells (10:1 ratio) into nu/nu mice and scored at necropsy (E, F). Data are the mean ± SD from a single experiment incorporating biological replicate samples (n = 3, unless otherwise indicated) and are representative of at least 2 independent experiments. Two-tailed Student's t test (B and C). One-way ANOVA test (E and F).

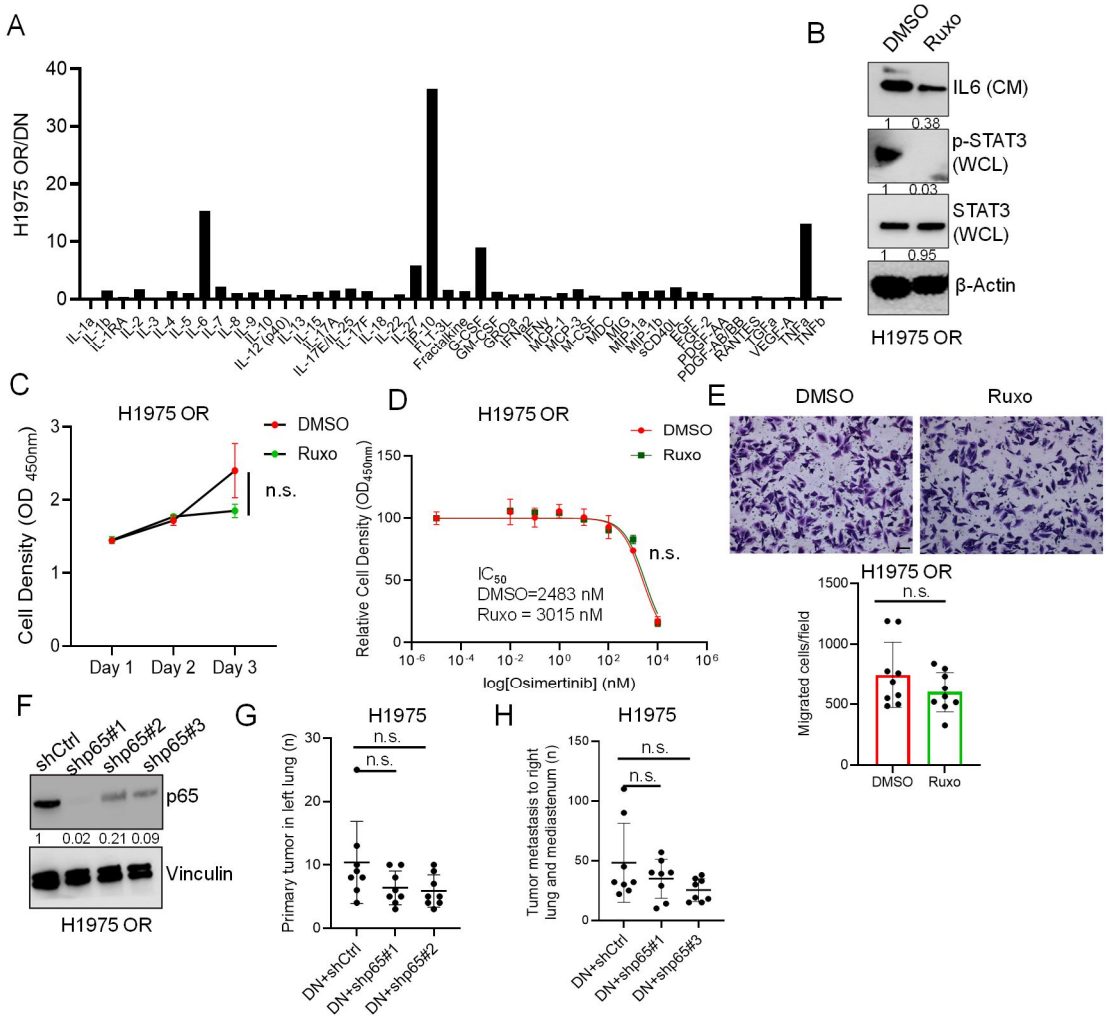

Figure 3. Senescence-activated cytokine secretion in H1975 OR cells. (A) Fold change of Cytokine concentrations in conditioned medium (CM) samples quantified by multiplexed antibody-based bead assays. Results expressed as a ratio (OR:DN). (B) Western blot (WB) analysis of H1975 OR cells treated with 0.5μM of the Janus kinase inhibitor Ruxolitinib (Ruxo) to inhibit senescence-activated secretion. p-STAT3 levels in WCL included as positive control for drug target inhibition Vehicle DMSO control. (C, D) Relative densities of H1975 OR cells treated with Ruxo alone (C) or in combination with varying doses of Osi (D). (E) Boyden chamber migration assays on H1975 OR cells treated with Ruxo. Results expressed as an average number of migrated cells per field. Scale bars 1 mm. (F) WB analysis confirming target gene depletion in shRNA-transfected H1975 OR cells. shCtrl, control. Vinculin loading control (G, H) DN cells were injected in combination with cells described in (F) (10:1 ratio) into nu/nu mice. At necropsy, each mouse (dot) was scored based on primary lung tumor numbers (G) and mediastinal lymph node and contralateral lung tumor metastases (H). Data are the mean ± SD from a single experiment incorporating biological replicate samples (n = 3, unless otherwise indicated) and are representative of at least 2 independent experiments. Two-way ANOVA test (C and D). Two-tailed Student's t test (E). One-way ANOVA test (G and H).

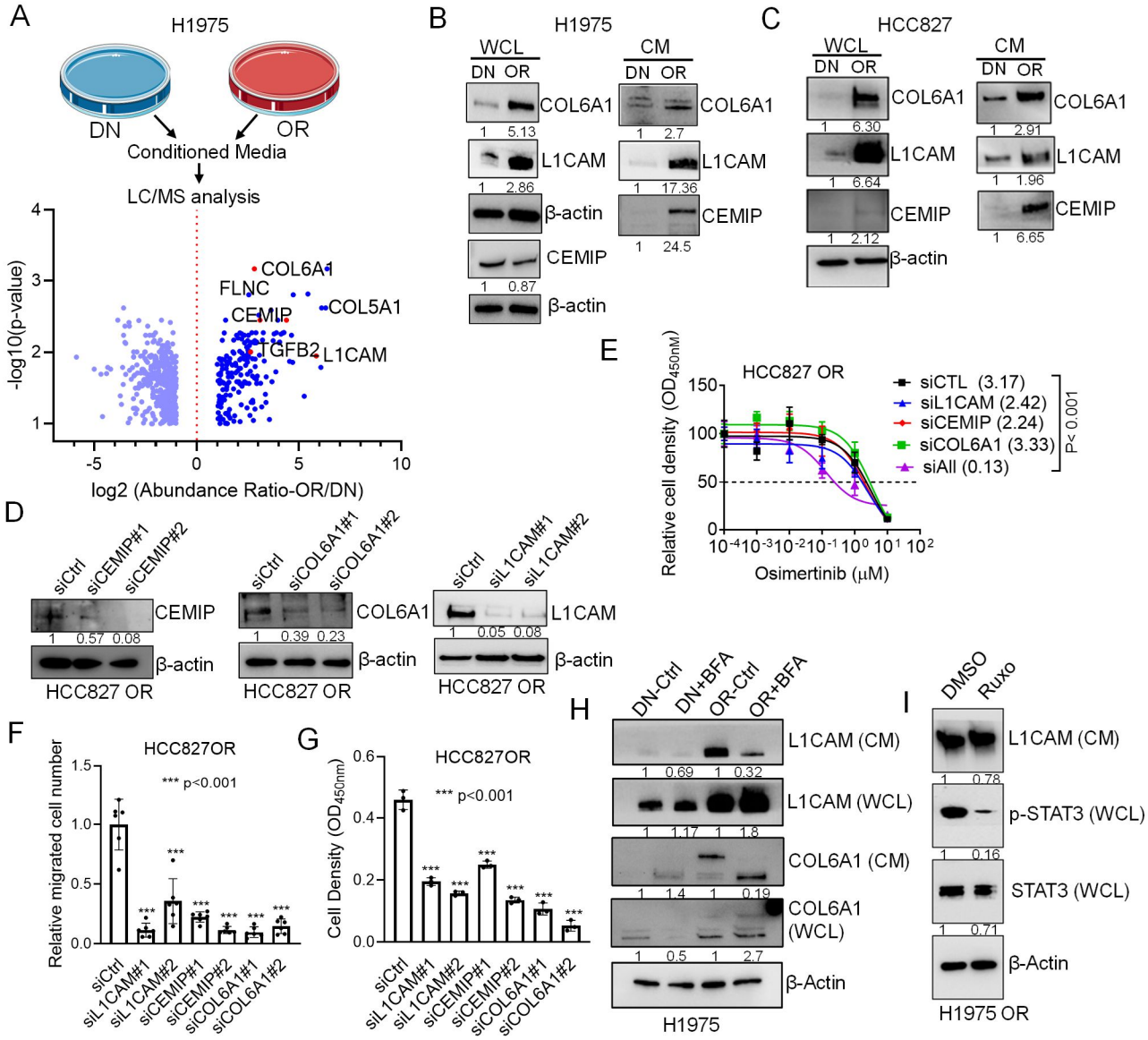

Figure 4. Identification of secretory mediators in H1975 OR cells. (A) Volcano plot of proteins identified by LC-MS analysis of CM samples isolated from H1975 cells (DN or OR). Proteins (dots) plotted by P value (y axis) and fold change (x axis). Fold change>2, p <0.05. Proteins of interest are labeled. (B, C) WB analysis of secreted proteins of interest in whole cell lysate (WCL) and CM samples from H1975 cells (DN or OR) (B) or HCC827 cells (DN or OR) (C). β-actin loading control. (D) WB confirmation of target gene depletion (CEMIP, COL6A1, or L1CAM) in siRNA-transfected HCC827 cells. siCtrl, control. β-actin loading control. (E) Relative densities of siRNA-transfected HCC827 OR cells following 4 days of Osimertinib treatment in monolayer culture. IC50 values were calculated. (F) Boyden chamber migration assays on siRNA-transfected cells. Results expressed relative to siCtrl. (G) Relative densities of siRNA-transfected HCC827 cells in monolayer culture quantified at day 4. (H) WB analysis of L1CAM and COL6A1 in CM and WCL samples following treatment with brefeldin A (10 μg/ml) for 4 h in H1975 DN and OR cells. (I) WB analysis of L1CAM in CM samples from H1975 OR cells after 24 h treatment with 1μM Ruxo. p-STAT3 levels in WCL included as positive control for drug target inhibition. Data are the mean ± SD from a single experiment incorporating biological replicate samples (n = 3, unless otherwise indicated) and are representative of at least 2 independent experiments. Two-way ANOVA test (E). One-way ANOVA test (F and G).

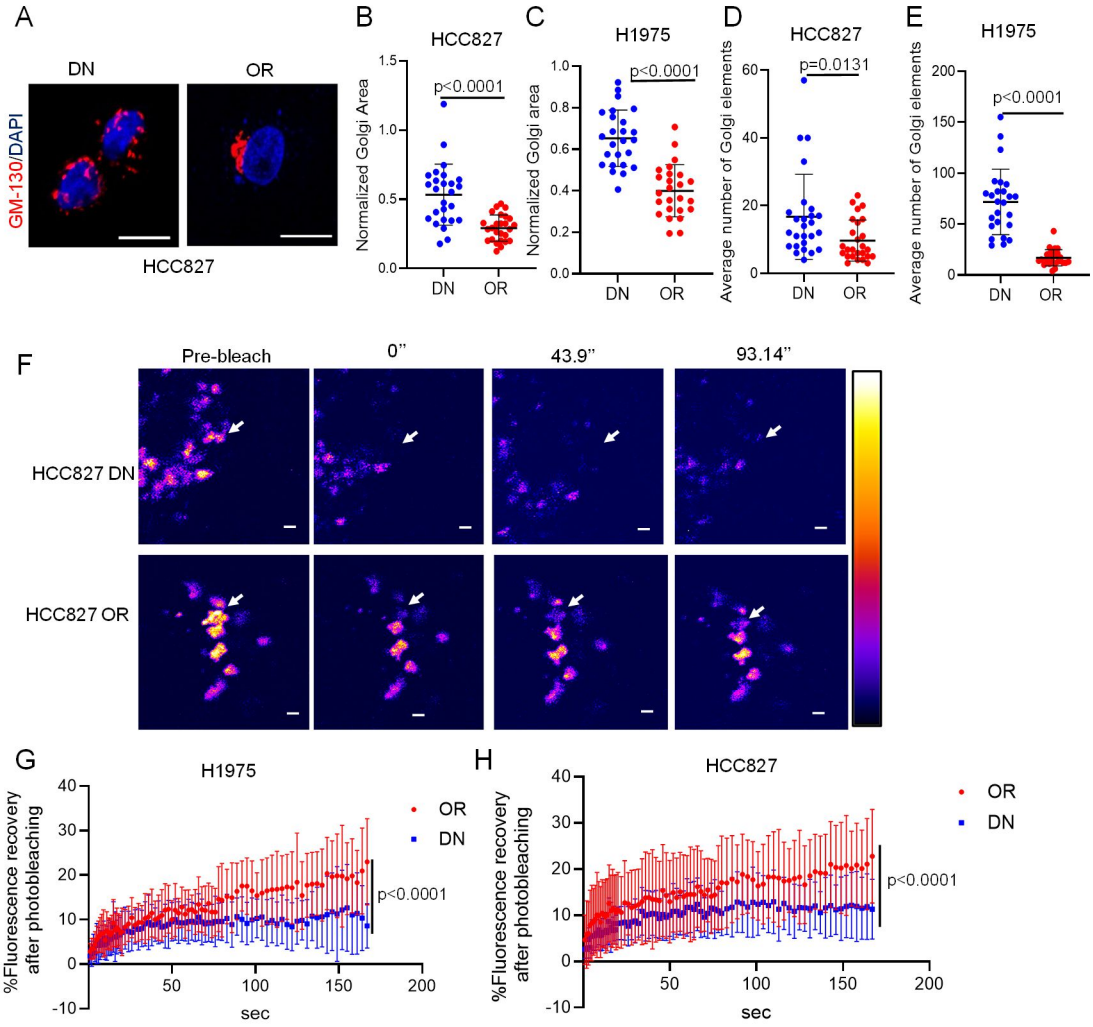

Figure 5. Distinct Golgi dynamics in OR cells and DN cells. (A) Confocal micrographs of anti-GM130 antibody-stained HCC827 cells (DN and OR). Golgi (red). Nuclei (DAPI, blue). Scale bars: 10 μm. (B, C) Scatter plots of Golgi area per cell (dot) in HCC827 cells (B) and H1975 cells (C). Values were normalized to nucleus area. (D, E) Scatter plots of Golgi element numbers per cell (dot) in HCC827 cells (D) and H1975 cells (E). (F) Fluorescence recovery after photobleaching (FRAP) assays. Pseudo-colored images of the Golgi enzyme GalNAcT at indicated time points after photobleaching. Bleached regions of interest (arrows). Intensity levels are indicated by a lookup (LUT) table bar (right). Scale bars: 1 μm. (G, H) Scatter plot of intensity recovery after photobleaching (%) in H1975 cells (G) and HCC827 cells (H). Each dot represents a mean value from n = 14 cells per group. Data are the mean ± SD from a single experiment and are representative of at least 2 independent experiments. Two-tailed Student's t test (B-E). Two-way ANOVA test (G and H).

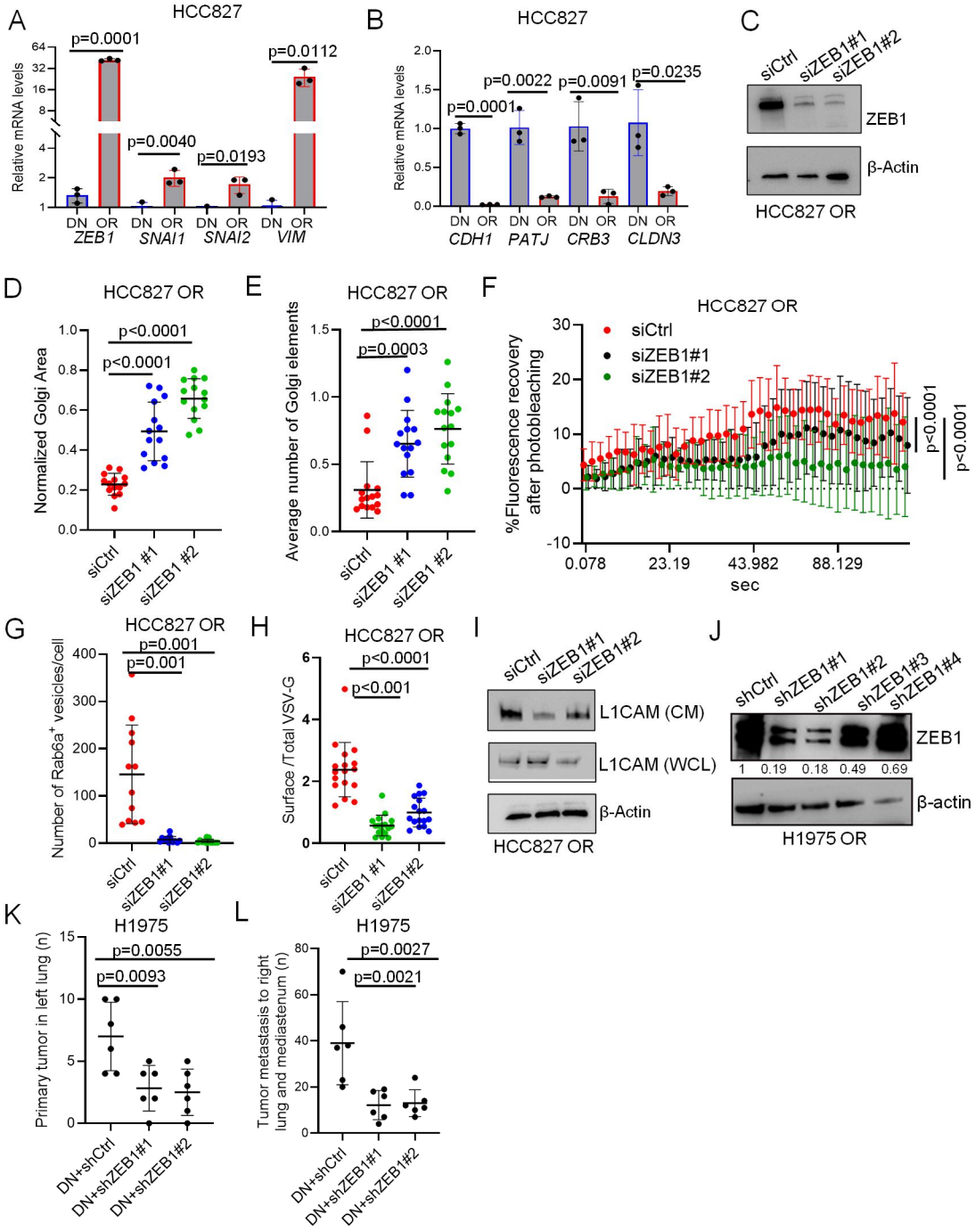

Figure 6. EMT drives Golgi and secretory dynamics in OR cells. (A, B) Quantitative PCR analysis of mRNA levels in HCC827 cells (OR and DN). Relative levels of EMT-activating transcription factors (ZEB1, SNA1, SNAI2), and mesenchymal marker VIM (A). Relative levels of epithelial polarity complex components (CDH1, PATJ, CRB3, and CLDN3) are indicative of EMT in OR cells(B). (C) WB confirmation of siRNA-mediated target gene depletion in HCC827 OR cells. β-actin loading control. (D) Scatter plot of Golgi areas per siRNA-transfected cell (dot). Values normalized to nucleus area. (E) Scatter plot of Golgi element numbers per cell (dot). (F) Scatter plot of intensity recovery (%) after photobleaching (n = 10 cells per group). (G) Quantification of Rab6A$^+$ vesicles per cell (dot). Vesicles identified based on GFP-tagged Rab6A reporter activity. (H) Ratio of surface-to-total VSV-G per cell (dot) infected with Ad-EGFP-VSV-G and imaged 30 min after transfer to 32 °C. (I) WB analysis of L1CAM in CM and WCL samples. (J) WB confirmation of shRNA-mediated target gene depletion in H1975 OR cells. β-actin loading control. (K, L) DN cells were injected in combination with cells described in (J) (10:1 ratio) into nu/nu mice. At necropsy, each mouse (dot) was scored based on primary lung tumor numbers (K) and mediastinal lymph node and contralateral lung tumor metastases (L). Data are the mean ± SD from a single experiment incorporating biological replicate samples (n = 3, unless otherwise indicated) and are representative

of at least 2 independent experiments. Two-tailed Student's t test (A and B). One-way ANOVA test (D, E, G, H, K, and L). Two-way ANOVA test (F).

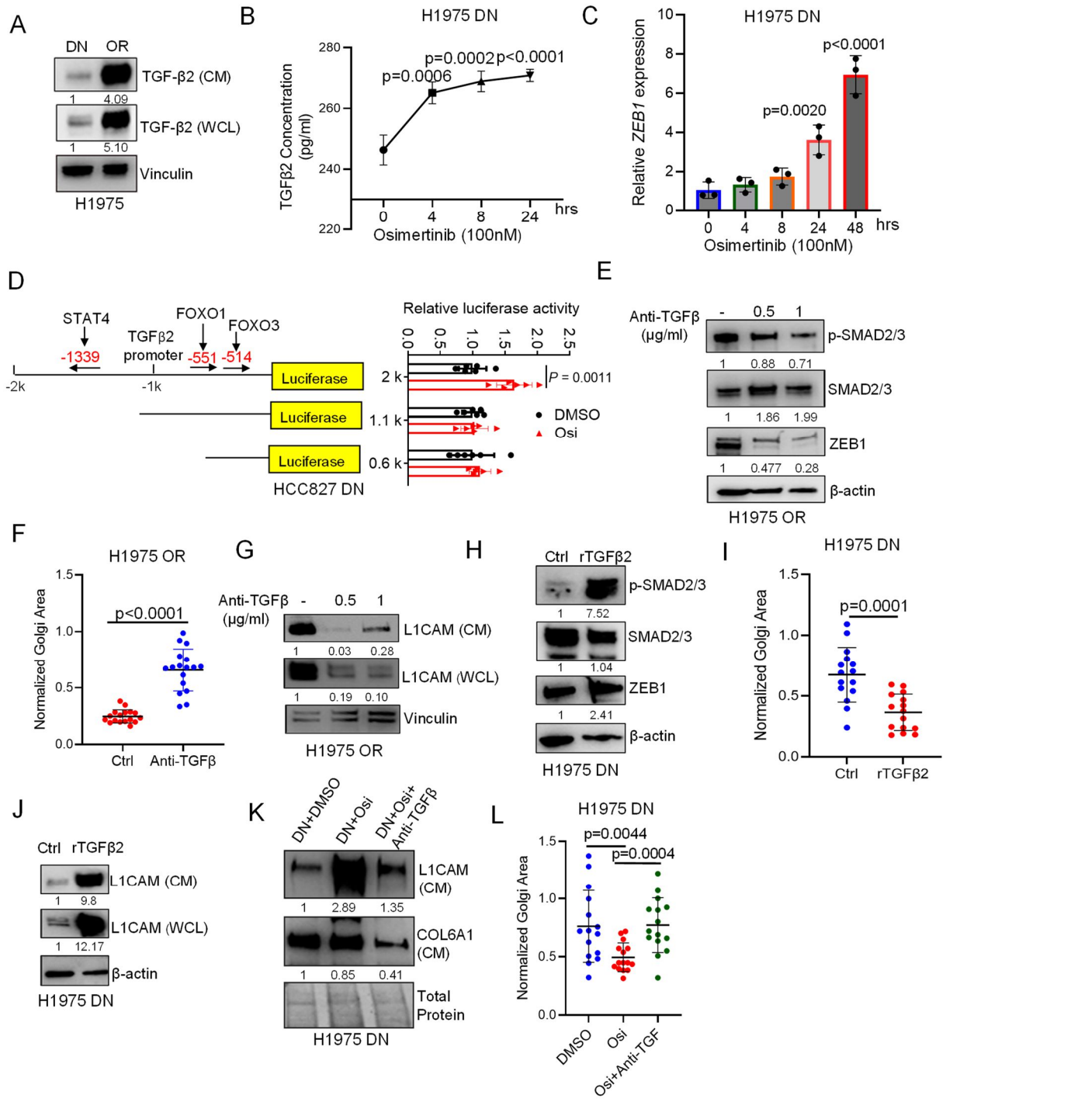

Figure 7. Osimertinib activates TGFβ2 secretion to initiate the EMT-dependent secretory pathway. (A) TGFβ2 WB analysis of CM and WCL samples from H1975 cells (DN or OR). (B) Enzyme-linked immunosorbent assays of CM samples show that increased TGFβ2 secretion is detectable 4 h after initiating Osimertinib treatment in H1975 DN cells. (C) Quantitative PCR analysis shows that ZEB1 mRNA levels are upregulated 24 h after initiating Osimertinib treatment in H1975 DN cells. (D) TGFβ-2 gene promoter reporter assays. Reporters containing a 2 Kb TGFβ2 gene promoter fragment or truncated (1.1 Kb or 0.6 Kb) fragments were transfected into HCC827 DN cells. After 48 h, cells were treated with DMSO or 100 nM Osimertinib for 24 h. Values were Renilla-normalized, averaged from replicates (n=6), and expressed relative to DMSO. Predicted transcription factor binding sites shown in schematic (left). (E) WB confirmation of SMAD2/3 dephosphorylation by 0.5 and1 ug/ml neutralizing anti-TGFβ antibody treatment of H1975 OR cells. β-actin loading control. (F) Scatter plot of Golgi areas following TGFβ neutralization in H1975 OR cells (dots). Values normalized based on nucleus area.

(G) WB analysis of L1CAM in CM and WCL samples following TGFβ neutralization in H1975 OR cells. (H) WB confirmation of increased SMAD2/3 phosphorylation by 100nM recombinant TGFβ2 treatment of H1975 DN cells. β-actin loading control. (I) Golgi areas following recombinant TGFβ2 treatment in H1975 DN cells (dots). Values normalized based on nucleus area. (J) WB analysis of L1CAM in CM and WCL samples following recombinant TGFβ2 treatment of H1975 DN cells. (K) WB analysis of L1CAM and COL6A1 in CM samples from H1975 DN cells treated for 24 h with DMSO, 100nM Osimertinib or Osimertinib in combination with 1ug/ml neutralizing anti-TGFβ antibody. Ponceau-stained gel included as loading control. (L) Scatter plot of Golgi areas in H1975 DN cells (dots) treated with Osimertinib alone or in combination with neutralizing anti-TGFβ antibody. Data are the mean ± SD from a single experiment incorporating biological replicate samples (n = 3, unless otherwise indicated) and are representative of at least 2 independent experiments. One-way ANOVA test (B, C, and L). Two-tailed Student's t test (D,F, and I).